

# Virtual Hyperspectral Images and Spectral Feature Extraction Using Symmetric Autoencoders

Archisman Bhattacharjee, Pawan Bharadwaj, Laurent Demanet

**Abstract**—Spectral data acquired through remote sensing are invaluable for environmental and resource studies. However, these datasets are often marred by nuisance phenomena such as atmospheric interference, sensor noise and other complexities, posing significant challenges for accurate analysis. We show that an autoencoder architecture, called symmetric autoencoder (SymAE), which leverages symmetry under reordering of pixels, can learn to disentangle the influence of nuisance features from class-invariant spectral features on a pixel-by-pixel basis. This disentanglement is achieved through a purely data-driven process, obviating the need for transfer models, noise distribution priors, or reference ‘clean signals.’ Additionally, SymAE can generate virtual hyperspectral images by manipulating the nuisance effects of each pixel. Using AVIRIS instrument data, we demonstrate that these virtual images are valuable for subsequent image analysis tasks. The extraction of invariant spectral features within classes, enabled by SymAE, also positions it as highly effective in clustering and classification tasks. We demonstrate this by delivering state-of-the-art classification results for a purely spectral method across four popular benchmark HSI datasets.

**Index Terms**—autoencoders, deep learning, hyperspectral imaging, nuisances, redatuming, virtual images, spectral feature extraction, hyperspectral image classification

## I. INTRODUCTION

Complications due to nuisance or uninteresting parameters arise in many inverse problems. In remote sensing of the Earth’s surface, nuisance effects could be associated with atmospheric effects, sensor noise, sun-angle variations, topographic effects, spatial intra-class variations, spectral mixing, and instrumental and data artifacts [1], [2]. The presence of such nuisance can make the inference of useful surface reflectance features highly uncertain. Therefore, dealing with these nuisance effects is seen as a critical pre-processing step.

Over the years, several methods have been developed to address the specific challenges associated with these nuisances in hyperspectral images (HSI). The inherent complexity of hyperspectral data, characterized by its high dimensionality and diverse interference types, hinders these processes [3]. A major challenge is the selection of appropriate noise distribution priors for algorithms, a task made tricky by the variable nature of interference across different hyperspectral scenarios, including types that may display nonlinear characteristics [4], [5]. Model-driven strategies, relying on predefined

models, offer interpretability but are often limited by their sensitivity to parameter adjustments in different hyperspectral settings. Data-driven approaches, particularly those employing deep learning, provide adaptability but struggle due to the scarcity of clean reference images for training [6]. Recently, some model-data-driven denoising approaches have been developed, combining the strengths of both model-based and data-driven methodologies to enhance robustness and achieve commendable results in noise reduction [7], [8], [9]. Yet,

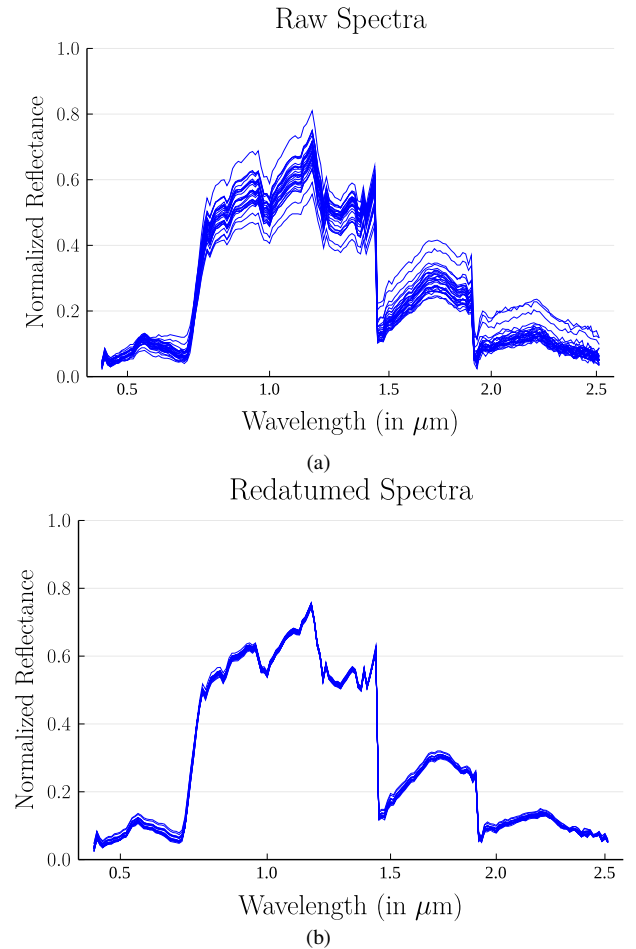


Fig. 1. Example from the Kennedy Space Center dataset. (a) Original spectra in the dataset belonging to Oak Hammock vegetation class. These pixel spectra showcase dissimilarities possibly arising from nuisance effects like atmospheric or ground-based variations. (b) The raw spectra undergo the redatuming process to generate virtual spectra, as depicted here. Through redatuming, the spectra share nuisance effects, leading to uniformity among spectra while preserving vegetation-class-specific reflectance features.

Manuscript received 26th September, 2023; revised 15th February, 2024; (Corresponding author: Archisman Bhattacharjee.)

Archisman Bhattacharjee and Pawan Bharadwaj are with Centre for Earth Sciences, Indian Institute of Science, Bangalore, India.

Laurent Demanet is with Dept. of Mathematics and Earth Resources Laboratory, Massachusetts Institute of Technology, Cambridge, USA. (e-mail: archismanb1999@gmail.com; pawan@iisc.ac.in; ldemanet@mit.edu)

these approaches still hinge on simulated noisy images with assumptions about noise distribution types paired with clean reference images, potentially limiting their applicability in uncharted settings. Similarly, atmospheric correction methods face challenges, as they work to accurately model atmospheric interactions under diverse conditions [10], [11]. These issues highlight the need for an approach that can more effectively adapt to the complexities of hyperspectral data and enhance image analysis tasks.

In this note, we demonstrate the utility of an autoencoder [12], [13] architecture, called the symmetric autoencoder (SymAE) [14], to disentangle nuisance features from surface reflectance features in its latent space. Additionally, SymAE enables the generation of virtual spectra with selected nuisance conditions, a process we term ‘redatuming’, borrowing from seismic imaging terminology [15]. While atmospheric correction methods aim to compensate for atmospheric effects, and denoising methods attempt to estimate the ‘noise-free’ HSI counterparts [4], we present a distinct approach. Through redatuming, we can *uniformize* nuisance effects across spectra, mitigating the ambiguity of identifying a ‘noise-free’ image in the absence of clean references. This approach reduces speculative noise assumptions while still facilitating various analysis tasks. To illustrate this, envisage a collection of pixels belonging to a specific class. Among these, certain pixels might be obscured by cloud cover, while others enjoy the clarity of an unobstructed sky. Through redatuming, nuisances can be transposed from one pixel to another, effectively generating virtual pixel spectra. These synthesized pixels can be systematically manipulated to simulate either cloudless or cloudy conditions — effectively aligning pixels in terms of their nuisance effects as shown in Fig. 1.

SymAE constitutes an encoder that provides a compressed latent representation of the input hyperspectral image on a pixel-by-pixel basis and a decoder that reconstructs the input in a near-lossless manner. The latent representation of this autoencoder is valuable because each at-sensor pixel spectrum is decomposed into two components (dimensions): one correlated to nuisance parameters and another to the surface reflectance features. Specifically, a disentangled representation can be used to manipulate the nuisance information of the pixels, e.g., the swapping of the atmospheric effects of a given pixel with another. As will be discussed later, swapping nuisance effects is equivalent to decoding a hybrid latent code prepared by mixing components of the latent code between the respective pixels. Consequently, the nuisance effects can be uniformized across the pixels, producing a new virtual hyperspectral image. It should be crucially emphasized that the SymAE executes the aforementioned decomposition in a model-free manner, excluding the need for prior information about nuisance parameters.

Traditional autoencoding ideas alone will not guarantee that the surface reflectance features and nuisance features of an input spectrum are encoded as separate components in the latent space. To accomplish data-driven representation learning, we harness the property of permutation invariance found in surface reflectance of pixels with common features. In other words, when examining a group or a cluster of pixels

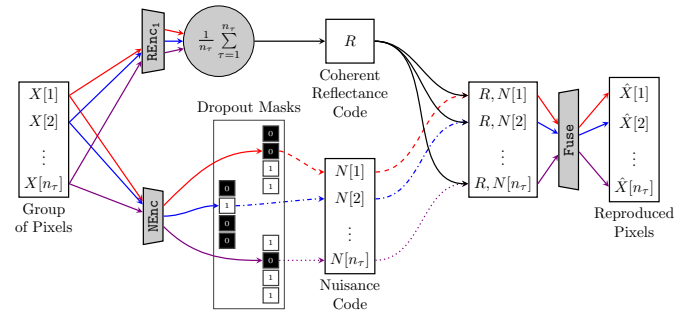


Fig. 2. The architecture of a symmetric autoencoder disentangles surface reflectance information from the nuisance (for example, atmospheric scattering) effects in its latent space. The surface-reflectance information is assumed to be coherent across the pixels in a group. Therefore, it can only propagate through the network via solid arrows — notice that the dropout masks prevent its propagation. Colored arrows indicate the propagation of the remaining nuisance effects — notice that a symmetric function, i.e., symmetric w.r.t. the ordering of pixels, prevents its propagation.

within extensive remote-sensing datasets, possessing identical surface-reflectance information — this information remains unaffected by the arrangement or the ordering of pixels within this group. Specifically, we capitalize on grouping the observed spectra a priori to structure the latent space. The identification of these groups is application-specific, and some ideas are discussed in Section II. Finally, the latent representation of the SymAE is guided by specific constraints linked to these grouped spectra, encompassing:

- Firstly, the surface-reflectance characteristics within a particular group exhibit symmetry concerning the arrangement of its spectra. In essence, the surface reflection information is assumed to be coherently shared across the spectra within the group.
- Secondly, the nuisances across the spectra within a given group are distinct, i.e., each spectrum experiences a distinct unwanted alteration, influenced by corresponding nuisance phenomena. For example, pixels within a group containing effects due to diverse atmospheric configurations.

These constraints collectively steer SymAE’s learning process, facilitating the creation of a latent representation that captures the essential features while accounting for the complexities introduced by nuisances. SymAE training is a highly generalized form of blind deconvolution that uses the merging of different latent variables in a neural network to replace the notion of convolution. The architectural design choices of SymAE, which are made to ensure that the constraints mentioned above are satisfied, are detailed in [14].

### Surface Reflectance and Nuisance: Contextual Clarification

Before we delve further, we wish to underscore the nuanced nature of the term *surface-reflectance*, which we will consistently employ throughout the remainder of this article. Although we assert our intention to disentangle these features from the spectra, we are, in fact, more accurately extracting *coherent features* from within spectral groups. To illustrate

this, consider a collection of spectra obtained through multi-scan hyperspectral imaging of a specific location at various instances, each affected by diverse atmospheric conditions. In this context, the repeated measurement of reflectance from identical surface constituents ensures that surface information remains coherent across pixels. It is worth noting here that while the term ‘coherent features’ might seemingly overlap with surface-reflectance features, certain atmospheric attributes could exhibit coherency across multiscan measurements. Additionally, surface reflectance might undergo seasonal changes, e.g., due to variations in surface moisture content, etc. However, due to the inherent challenge of physically labeling the coherent information and the fluidity of coherency based on the application context, we will frequently use the term ‘surface reflectance’ when discussing concepts in this paper. It is crucial to recognize that within the framework of SymAE, the classification of information into coherent information and nuisance information depends on the strategies used for grouping. This paper highlights the advantages of disentangling the coherent information through spectral grouping for classification and surface characterization tasks, in contrast to working with the raw spectra.

#### *SymAE: A Potent Spectral Feature Extractor*

In hyperspectral imaging, feature extraction plays a crucial role in converting complex, high-dimensional spectral data into meaningful and concise features. This transformation is key for effective analysis in applications like environmental monitoring, precision agriculture, and urban planning. As spectral features offer the main discriminative power in HSIs [16], efficient extraction of these features is of significant interest. Deep learning-based methods have shown significant advancement in HSI classification tasks. However, Hong *et al.* [17] identified limitations in architectures like convolutional neural networks (CNNs), recurrent neural networks (RNNs), graph convolutional networks (GCNs), and others in extracting sequential information. In their work, they introduced Transformer-based architectures [18], [19] to efficiently extract spectral features and achieve state-of-the-art classification performance. This inspired other Transformer-based architectures [20], [21], [22], with some incorporating spatial information for higher accuracy.

While SymAE is not a Transformer-based architecture, its architectural constraints make it a valuable spectral feature extractor. Particularly, the permutation invariance constraint in SymAE enables it to capture class-specific invariant features, which are disentangled from nuisance features. Leveraging these features, we achieve state-of-the-art classification results for a purely spectral method across four standard HSI datasets: Kennedy Space Center, Pavia University, Indian Pines and Houston2013. These results are detailed in subsection IV-D. This capability offers significant potential for diverse applications, including land cover identification, mineral characterization, and spectral signature analysis.

#### *Contributions*

The main contributions through this paper can be summarized as:

- 1) We introduce a deep learning autoencoder architecture for hyperspectral imaging, designed to disentangle nuisance features from class-specific reflectance features in a purely data-driven manner. This architecture also facilitates the generation of virtual spectra, allowing for the simulation of different nuisance scenarios on a pixel-by-pixel basis.
- 2) Distinct from traditional atmospheric correction or denoising methods, we introduce a novel approach that utilizes virtual hyperspectral images with uniformized nuisances through redatuming. This method bypasses the need for prior assumptions about noise distribution and the reliance on reference clean images, offering potential advantages in uncharted environments. While a direct comparison with other denoising methods is not straightforward due to differing objectives, we demonstrate the utility of these virtual images for subsequent image analysis tasks.
- 3) We demonstrate SymAE’s effectiveness as a spectral feature extractor, adept at capturing class-specific invariant features. This functionality is particularly beneficial for tasks such as clustering, classification, and segmentation. In our classification experiments, SymAE gives state-of-the-art performance for a purely spectral method across four benchmark datasets.

Before advancing to the next section, we highlight the difficulty in comparing our method, SymAE, with other denoising methods. Standard Signal-to-Noise Ratio (SNR) tests, commonly used to assess denoising methods, are not well-suited for evaluating SymAE due to its unique operational focus. Contrary to typical denoising approaches that aim at visual image enhancement, SymAE is designed for disentangling nuisance features from class-specific reflectance features in spectra, a fundamentally different task. Additionally, SNR assessments usually require a reference ‘clean’ image, which is not always applicable for SymAE. The primary goal of SymAE is representation learning, often without a direct clean reference. Therefore, the effectiveness of SymAE is more accurately measured using metrics related to classification accuracy, clustering quality, or the ability to identify subtle spectral variations, rather than SNR. We also acknowledge the work of Liu *et al.*, who used a normalized flow-based [23] network architecture for disentangling noise distribution from clean image distribution [24]. This approach is similar to ours in terms of representation learning and disentanglement, but they use known clean and noisy image pairs and focus on general imaging, unlike our specific application in HSI.

## II. SPECTRAL GROUPING

Our approach necessitates a priori grouping of spectra to effectively disentangle nuisance effects. All the spectra in a given group are presumed to contain identical coherent information but dissimilar nuisance effects. The number of such identifiable groups is the application and scene-specific. If we intend to disentangle atmospheric and lighting variations from surface reflectance, an ideal scenario for achieving this objective is one in which multi-scan hyperspectral data is

available. In this setup, each pixel undergoes multiple scans under diverse atmospheric conditions and varying elevation angles. Here, each group of spectra pertains to the same pixel but exhibits varying atmospheric influences. In this context, SymAE shows promise for disentangling atmospheric nuisances and pixel-specific reflectance in an entirely unsupervised manner.

Acknowledging the challenges in acquiring multi-scan data for real-world applications, we concentrate instead on single hyperspectral scenes. The grouping task is straightforward if distinct spatial features (e.g., water bodies, crops, asphalt, etc.) are identifiable in the image. In addition, pixels that are classified with high certainty during a preliminary analysis can also assist the grouping task. Specifically, our approach in this paper involves grouping pixels using a priori information derived from two sources: 1) ground truth labeling and 2) spatial proximity. Leveraging ground truth information entails forming groups based on assigned pixel classes, such as specific vegetation or land types, in hyperspectral images. Note that the variations in textures, spectral mixing, and other atmospheric factors exist even among pixels of the same class, contributing to what we refer to as nuisance effects. During training, we utilized approximately 10% of the ground truth information. We showcase its performance on the remaining test pixels of the scene in Section IV. In cases where ground truth labels are limited, we adopt an alternative approach by working with groups of spatially proximate pixels (groups of 9 pixels, present in  $3 \times 3$  patches). Here, SymAE is trained to extract spatially-coherent features. Although we acknowledge that this spatial grouping method is less efficient than using ground truth, we analyze its advantages in Section V.

A hyperspectral image is inherently three-dimensional, with the first two dimensions representing the spatial domain, and the third dimension corresponding to the spectral domain. To facilitate our analysis, we group pixels into distinct sets, bundling together all pixels belonging to the same group. These grouped pixels are utilized for training our autoencoder after constructing a set of datapoints denoted as  $\{X_i\}_{i=1, \dots, n_X}$ . Each datapoint,  $X_i$ , comprises a selection of pixels randomly drawn, with replacement, from the same group. The datapoints are assigned to all the available groups uniformly. In our notation,  $[A; B]$  signifies the vertical concatenation of two vectors,  $A$  and  $B$ . To access individual pixels within a datapoint, we index them as  $X_i[\tau]$ , where  $\tau$  ranges from 1 to  $n_\tau$ . Consequently,  $X_i$  is constructed as  $[X_i[1]; \dots; X_i[n_\tau]]$ . Each pixel spectrum, represented by  $X_i[\tau]$ , is a vector of length equal to the number of frequency bands. These constructed data points serve as the basis for training SymAE, with further details provided in the subsequent section.

### III. SYMMETRIC AUTOENCODER

We constructed the datapoints such that the surface reflectance is *coherent* across the pixels of each datapoint. The goal of symmetric autoencoder [14] is to disentangle this coherent reflectance information from the remaining nuisance variations, e.g., atmospheric effects, in its latent space. Autoencoders [25] are comprised of two components: an encoder Enc

that maps each datapoint  $X_i$  into latent code  $H_i = \text{Enc}(X_i)$ , and a decoder Dec that attempts reconstruct to  $X_i$  from the code. We determine both the functions Enc and Dec by minimizing the reconstruction loss

$$\text{Enc, Dec} = \arg \min_{\text{Enc, Dec}} \sum_i \|X_i - \text{Dec}(\text{Enc}(X_i))\|^2 \quad (1)$$

over the training datapoints. SymAE relies on a unique encoder architecture, as depicted in Fig. 2, to structure the latent space. This architecture can be mathematically described by

$$\text{Enc}(X_i) = [\text{REnc}(X_i); \text{NEnc}(X_i[1]); \dots; \text{NEnc}(X_i[n_\tau])]. \quad (2)$$

As a result, the latent code  $H_i = [R_i; N_i[1]; \dots; N_i[n_\tau]]$  is partitioned into the following interpretable components of each datapoint  $X_i = [X_i[1]; \dots; X_i[n_\tau]]$ :

- 1) the component  $R_i = \text{REnc}(X_i)$  contains the surface-reflectance information as it is coherent across the pixels of  $X_i$
- 2) the remaining components  $N_i[\tau] = \text{NEnc}(X_i[\tau])$  complement  $R_i$  with pixel-specific nuisance information.

Finally, SymAE's decoder Fuse non-linearly combines code  $R_i$  with each pixel-specific code  $N_i[\cdot]$  to reconstruct the original datapoint pixel-by-pixel

$$\begin{aligned} \hat{X}_i &= \text{Dec}(H_i) = \text{Dec}([R_i; N_i[1]; \dots; N_i[n_\tau]]) \\ &= [\text{Fuse}([R_i; N_i[1]]); \dots; \text{Fuse}([R_i; N_i[n_\tau]])]. \end{aligned}$$

Here, no constraints are enforced on functions NEnc and Fuse as they are parametrized using fully-connected layers. On the other hand, to ensure REnc, the *reflectance encoder*, only encodes the coherent reflectance, we constrain it to be invariant under permutations of the pixels in  $X_i$ . In other words, for all permutations  $\Pi$  along the pixel dimension, we desire that

$$R_i = \text{REnc}(X_i) = \text{REnc}(X_i[\Pi(1:n_\tau)]) \quad (3)$$

purely represents the coherent information since  $R_i$  does not depend on the labeling of the pixels in  $X_i$ . Moreover, it is important to note that the nuisance effects, which are dissimilar across the pixels, cannot be encoded using REnc without significant loss of information.

SymAE's reflectance encoder explicitly achieves the invariance mentioned above using a permutation-invariant network architectures following [26] which provide universal approximation guarantees for symmetric functions. These architectures use pooling functions such as the mean or the max across the instances to ensure permutation invariance. In our experiments, the spectrum of each pixel is simply transformed using  $\text{REnc}_1$ , an unconstrained function parametrized using fully-connected layers, and mean taken along the pixel dimension

$$R_i = \left( \frac{1}{n_\tau} \sum_{\tau=1}^{n_\tau} \text{REnc}_1(X_i[\tau]) \right). \quad (4)$$

We emphasize that the key observation in this equation is that the mean of the *transformed instances*  $\text{REnc}_1(X_i[\tau])$  is symmetric with respect to the ordering of pixels. This ensures

that the desired symmetry (eq. 3) is achieved. SymAE’s nuisance encoder NEnc is unconstrained. This aspect is a significant concern as the decoder Fuse might tend to ignore the  $R_i$  component in favor of using purely  $N_i[\cdot]$  information for reconstruction.

As the purpose of NEnc is exclusively to encode pixel-specific nuisance information while disregarding surface reflectance, SymAE incorporates *dropout masks* during training via Bernoulli dropout [27] with a probability of  $p = 0.5$ :

$$N_i[\tau] = \text{Dropout}(\text{NEnc}(X_i[\tau])). \quad (5)$$

The dropout introduces random obfuscation to elements of  $N_i$ , making the decoder Fuse perceive the codes as dissimilar and hindering the reconstruction of coherent surface-reflectance information from  $N_i$ . While there is a continuous stream of information from REnc, the outputs of NEnc intentionally introduce noise, with certain features being randomly obfuscated. This compels Fuse to extract as much meaningful information as possible from  $R_i$ , which inherently contains coherent data. Over time, Fuse becomes adept at capturing all coherent information from REnc, with the remaining pixel features learned from  $N_i$  encoded by NEnc. At test-time, the entirety of the  $N_i$  code is sent unaltered into the decoder. Finally, the functions NEnc, REnc<sub>1</sub> and Fuse are trained concurrently by minimizing Eq. 1 with the dropout mechanism just described. The success of SymAE requires a sufficiently large number of pixels with *dissimilar* nuisance variations in each group to achieve the desired structure of the latent space.

### Virtual Hyperspectral Images

Using a trained SymAE network, we can generate a virtual hyperspectral image by redatuming each of the measured pixel spectra. The redatuming is performed pixel-by-pixel by swapping the nuisance effects in a given spectrum with a reference pixel. Precisely, to redatum the  $k$ th pixel spectrum  $D[k]$ , we first extract its reflectance code using REnc<sub>1</sub>( $D[k]$ ). We then fuse this code with the nuisance code of the reference spectrum (indexed using  $k_0$ ) to obtain a virtual spectrum

$$\hat{D}_{k_0}[k] = \text{Fuse}(\text{REnc}_1(D[k]); \text{NEnc}(D[k_0])), \quad (6)$$

which is not originally measured. Therefore, SymAE allows for *scanning* the area corresponding to pixel  $k$  with nuisance conditions present during the observation of pixel  $k_0$ . The virtual image  $\hat{D}_{k_0}$  is generated by collecting all the virtual spectra with similar nuisance effects.

## IV. TRAINING WITH GROUND TRUTH

In this section, we perform spectral grouping using ground truth information to showcase the application of SymAE. We utilize a hyperspectral image acquired by NASA’s AVIRIS instrument over the Kennedy Space Center (KSC), Florida, on March 23, 1996. The image has dimensions of  $512 \times 614$  pixels and comprises 176 spectral bands. While this dataset was corrected using the ATREM [28] method based on radiative transfer modeling, researchers [29] have highlighted the necessity for post-ATREM polishing due to errors in solar irradiance models and atmospheric parameter estimations. The

differences in spectral signatures among certain vegetation types may appear subtle. However, due to the presence of nuisance effects, these spectral signatures can exhibit notable discrepancies, even within pixels belonging to the same class. Consequently, the correction of residual nuisance effects, referred to as *polishing*, becomes imperative to ensure accurate discrimination of land cover in this environment.

To train SymAE, we partitioned the ground truth data using approximately a 9 : 1 test-train split ratio. Subsequently, we organized the training set pixels into groups corresponding to the ground truth categories. Our training process involved  $n_X = 524288$  data points, utilizing  $n_\tau = 8$  and a mini batch size of 256. The dimensions of the latent codes,  $R_i$  and  $N_i$ , were both set to 64. For further details regarding the configuration of the architecture, a Jupyter notebook notebook written in Julia using the Flux package [30] is shared on [https://github.com/archieb1999/SymAE\\_KSC](https://github.com/archieb1999/SymAE_KSC).

After completing training, we generated virtual spectra using Equation 6 with randomly selected reference pixels. The resulting vegetation spectra exhibited a notably reduced intra-class variance, suggesting the uniformization of nuisance effects across these spectra. This is visually demonstrated in Fig. 3, where the spectra display a significant decrease in intra-class variance after undergoing the redatuming process. The autoencoder not only exhibits a high degree of proficiency in redatuming within the training set, but the variance is also considerably reduced in the case of test ground truth pixels that were excluded during training. Furthermore, it is noteworthy that subtle inter-class differences are retained throughout the redatuming process. These findings underscore the motivation for utilizing the redatumed pixels in subsequent classification and characterization tasks.

To quantify the extent of nuisance effects among pixels within a specific ground truth class, we employ the metric of *average variance*. Initially, we calculate the variance in spectral reflectance for each band, followed by computing the average of these variance values. This average effectively represents the overall variance among all spectra belonging to a particular ground truth class. A higher average variance indicates that the pixels within the chosen class exhibit significant dissimilarities. Post-redatuming, we anticipate observing a reduction in variance. This reduction is apparent in Table I, which presents the average variance values both before and after redatuming with a random pixel. Notably, following the redatuming procedure, the residual average variance in the test pixels is consistently below 5% for the majority of the classes.

However, we wish to emphasize that the choice of reference pixel can significantly impact virtual spectra. In our approach of a priori grouping based on ground truth data, we recognize that nuisances are not confined to atmospheric and lighting effects but also encompass ground-based factors. These factors encompass spectral mixing, surface moisture content, and texture, among others, and they may add complexity to the virtual spectral analysis. It is noteworthy that these nuisance effects may affect different classes to varying degrees. For instance, marsh classes may be more susceptible to spectral variations due to surface water content than upland vegetation classes, potentially resulting in substantial fluctuations in

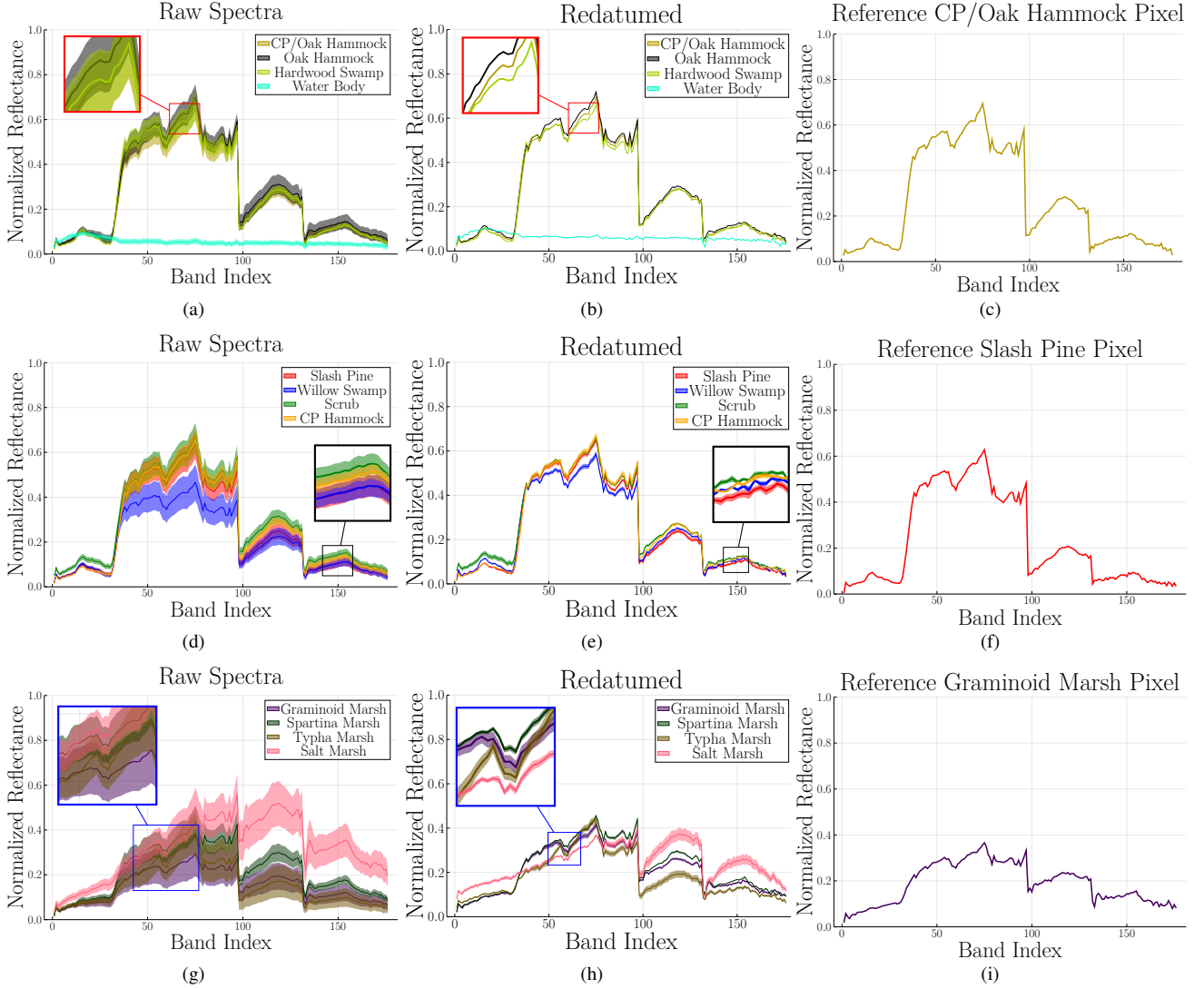


Fig. 3. Ribbon plots illustrate reduction in intra-class variance post-redatuning. Each ribbon plot represents spectral distribution of distinct classes, with central line denoting mean and ribbon's width on either side indicating intra-class standard deviation. (a) Displays train set spectra from four distinct classes, while (b) shows their respective redatuned counterparts, wherein pixels from the same classes almost coincide, and (c) shows the reference pixel used for redatuning. (d)-(f) Show spectra from test set upland vegetation classes, following the pattern observed in (a)-(c). While not as pronounced as in (b), the redatuned test set pixels exhibit a discernible reduction in intra-class variance. (g)-(i) are same as (d)-(f) but for wetland classes.

TABLE I  
Redatuning Significantly Reduces the Average Variance in Testing Pixels Across Diverse Ground Truth Classes in the KSC Dataset.

No.	Class	Training Samples	Test Samples	Average Variance In Raw Spectra ( $\times 10^{-6}$ )	Average Variance After Redatuning ( $\times 10^{-6}$ )	Residual Variance (%) After Redatuning
1	Scrub	77	684	1173.9	24.6	2.10 %
2	Willow Swamp	25	216	1938.3	17.0	0.88 %
3	CP Hammock	26	230	591.9	38.0	6.42 %
4	CP/Oak Hammock	26	225	1267.6	43.5	3.43 %
5	Slash Pine	17	144	1315.4	22.2	1.69 %
6	Oak Hammock	23	206	1346.5	61.5	4.57 %
7	Hardwood Swamp	11	94	695.3	9.4	1.35 %
8	Graminoid Marsh	44	387	3466.7	51.0	1.47 %
9	Spartina Marsh	52	468	1530.9	132.3	8.64 %
10	Typha Marsh	38	339	3086.0	141.1	4.57 %
11	Salt Marsh	42	377	3986.9	415.4	10.42%
12	Mud Flats	47	415	1529.5	325.1	21.26%
13	Water Body	91	817	143.0	0.047	0.03 %



energy reflected from marsh pixels. Additionally, some nuisance phenomena may pertain to specific classes but might not exist for others. For example, features related to crop ripeness may not be relevant in the context of water bodies. Thus, the degree of correspondence between generated virtual images and real-world scenarios may depend on the choice of reference pixel. Therefore, if the intention is to employ redatuming for detailed spectral and scenario analysis, we suggest selecting reference pixels with relatively similar nuisance feature distributions if prior information is available. Apart from a small example in the upcoming subsection, a detailed study on the interpretability of virtual spectra is beyond the scope of this paper. Instead, our primary focus in this paper is on the advantages of uniformizing nuisance features across spectra and extracting useful spectral features to enhance HSI analysis tasks.

#### A. Distinction from Denoising Autoencoders

Denoising Autoencoders (DAEs) represent a class of neural networks frequently employed in unsupervised learning. They are recognized for their proficiency in recovering underlying data representations by intentionally introducing noise into input data [31]. In the field of remote sensing and hyperspectral image analysis, various iterations of DAEs have been applied in previous studies [32]. In this study, we sought to compare the denoising effects of DAEs with that of redatuming by SymAE. Our observations indicate that while DAEs tend to smooth the spectral data, they fall short of significantly mitigating intra-class variance, as depicted in Fig. 4(b). DAEs typically assume a noise distribution, such as Gaussian, for denoising spectra. In contrast, SymAE adopts a different approach, implicitly learning the distribution of the underlying nuisance/noise after spectral grouping. Remarkably, SymAE

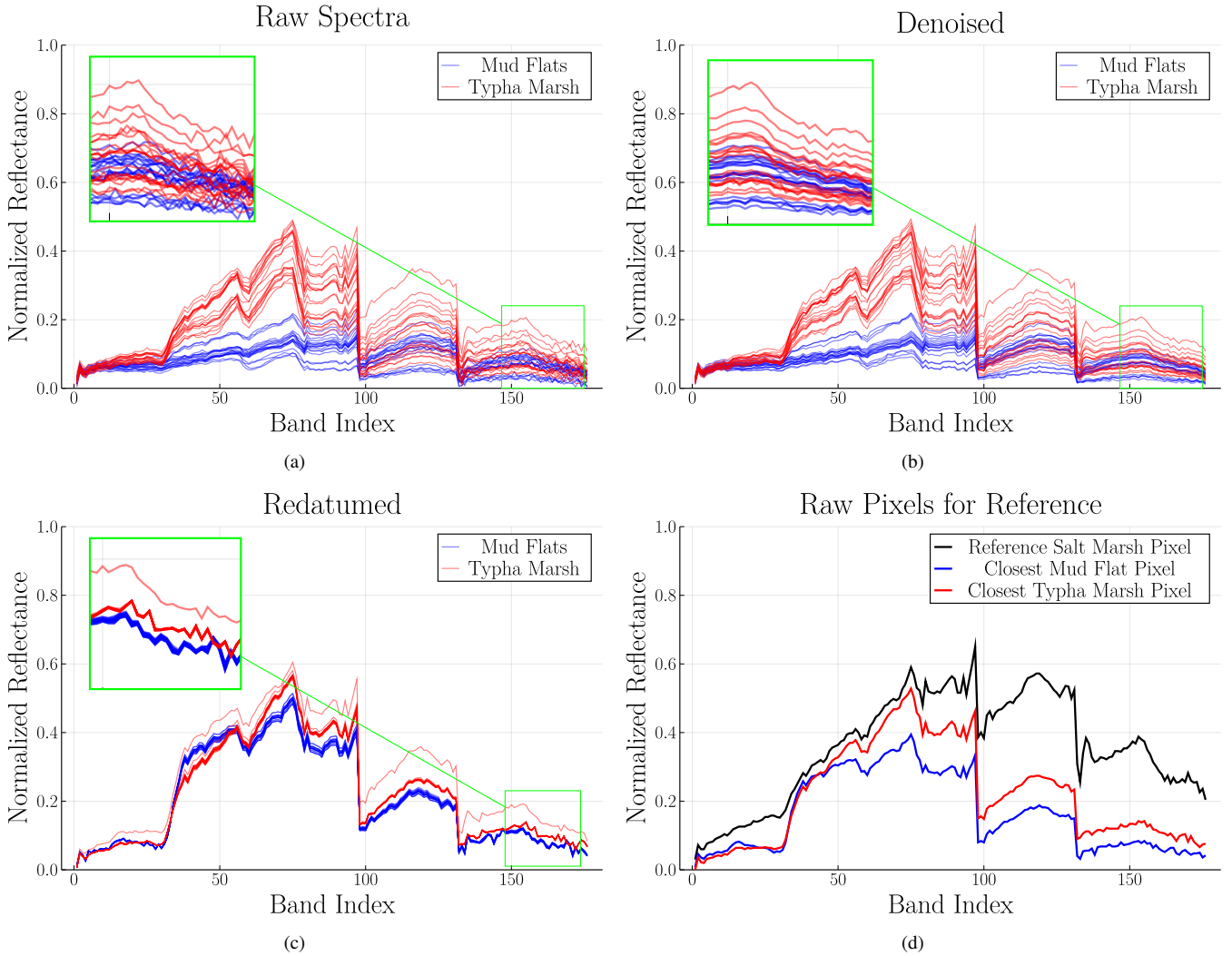


Fig. 4. Comparative analysis of application of DAE and SymAE on test data. (a) Raw spectra from two land-cover classes in Kennedy Space Center scene. (b) DAE demonstrates a propensity to smooth spectral data, yet notable within-group variations remain evident. (c) Redatuming, as implemented by SymAE, outperforms denoising by DAE in mitigating intra-class variance. However, it is important to note that redatumed spectra may exhibit significant dissimilarities from the original raw spectra. (d) Shows the reference Salt Marsh pixel used for the redatuming, along with pixels from the respective ground truth classes that are closest to the redatumed spectra.

significantly reduced intra-class variance, demonstrating its effectiveness in capturing and distinguishing distinctive features among classes. This attribute proves invaluable for tasks like classification and segmentation. However, it's important to note that virtual images may not be well-suited for tasks such as anomaly detection. SymAE may inadvertently treat anomalies as nuisances, with their details omitted in virtual spectra. Therefore, a more nuanced or alternative approach may be necessary for such tasks.

As mentioned earlier, it is important to recognize that the virtual spectra are contingent upon the reference pixel chosen during the redatuming process. While our demonstrations illustrate that a task such as classification remains relatively unaffected by the choice of this reference pixel, interpreting the virtual spectra may not be straightforward. These spectra are still influenced by the residual nuisance features present in the reference pixel. To illustrate this, we intentionally selected a Salt Marsh pixel with relatively high reflected energy (as shown in Fig. 4(d)) for redatuming Mud Flats and Typha Marsh pixels, as depicted in Fig. 4(c). Post-redatuming, the virtual spectra manifest noticeably elevated energy levels compared to their raw counterparts. This phenomenon likely stems from our autoencoder's incorporation of overall reflected energy as an element within the nuisance features. Nevertheless, the redatumed spectra still maintain a shape resembling the pixels closest to them in their respective ground truth classes, as referenced in subfigure 4(d). In essence, the SymAE-generated virtual images are not completely *denoised*; they still retain residual nuisance effects originating from the reference pixels. Nonetheless, due to the uniformity of nuisance features across the entire image, the relative distinctions among redatumed pixels can prove beneficial for subsequent image-processing tasks.

## B. Virtual Images: Classification

SymAE adds the ability to visualize hyperspectral image locations under different virtual conditions, potentially improving pixel classification accuracy and broadening the scope of hyperspectral image analysis. To exemplify the benefits brought about by redatuming and the uniformization of nuisance effects across pixels, we conducted K-Nearest Neighbor (KNN) classification, with  $K = 5$ , on both the raw and virtual hyperspectral images. These results are presented in Fig. 5. For the raw image, the overall accuracy for the test pixels from the ground truth stands at 81.6%, a lower figure primarily attributed to the presence of nuisance effects. However, when applied to the virtual images after the uniformization of nuisances, the overall accuracy elevates significantly to  $92.8 \pm 0.9\%$ . In a parallel approach, we assessed the performance of two classic machine learning models on our test set: 1) Random Forests and 2) linear Support Vector Machines (SVM). The outcomes distinctly underscore the significance of SymAE-generated virtual images: an evident enhancement in predictive overall accuracy (OA) for both Random Forests (e.g., 86.2% accuracy for raw images versus a noteworthy  $93.0 \pm 0.9\%$  overall accuracy for virtual image) and linear SVM classifiers (74.0% overall accuracy for raw images compared to a substantial  $85.8 \pm 4.9\%$  overall accuracy for virtual images). As a result, we conclusively establish that the application of SymAE redatuming proves beneficial when undertaking land-cover discrimination tasks.

While more complex models, such as the Random Forests and KNN, exhibit relatively consistent performance, the substantial variance in accuracy when employing a linear SVM on different virtual images highlights the decisive role of reference pixel selection in shaping classification outcomes. This influence is not uniform across all cases, with some reference pixels leading to remarkable enhancements while

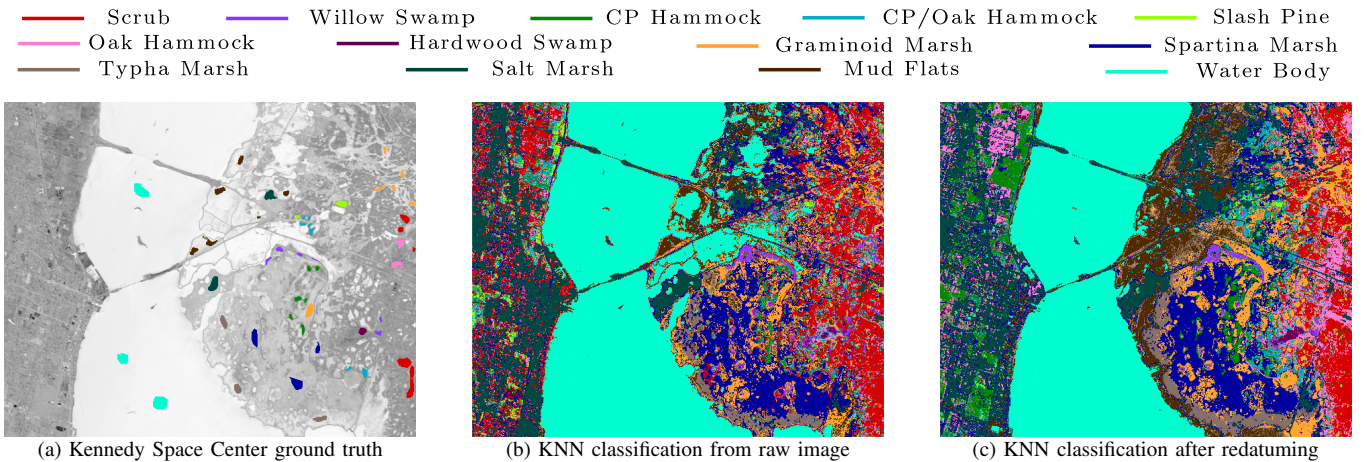


Fig. 5. K-Nearest Neighbors (KNN) pixel classification results on KSC scene maps. (a) ground truth map of the KSC scene, serving as the baseline. (b) Pixel classification utilizing KNN on the raw image, resulting in an overall accuracy of 81.6% for the test set ground truth. (c) Pixel classification conducted on a virtual image with uniformized nuisance, demonstrating an elevated average overall accuracy of 92.8%. Virtual images, generated through the redatuming process, contribute to enhanced pixel classification accuracy, highlighting their valuable role in advancing hyperspectral image analysis.



others, albeit rarely, induce performance deterioration. On average, our results demonstrate a significant overall improvement in classification performance. Nonetheless, the selection of an appropriate reference pixel can pose challenges. In subsequent sections, we introduce an alternative method for leveraging SymAE to further enhance clustering and classification.

### C. Surface-Reflectance Code: Clustering Analysis

The alternative method we mentioned is leveraging reflectance code generated by REnc for clustering and classification tasks. In addition to generating virtual images, a trained SymAE also provides us with a reflectance code, denoted as  $\text{REnc}_1(D[\cdot])$ , for each pixel. Since this code is intended to remain unaffected by atmospheric distortions and other forms of nuisance variability, the focus of this section is to leverage this code for clustering analysis. Our objective is to investigate whether the reflectance latent space can effectively disentangle classes characterized by subtle differences in reflectivity, such as neighboring vegetation types.

In the case of KSC experiment, we initially sampled 100 pixels from two ground truth classes, Slash Pine and Oak Hammock (Fig. 6(a)). We performed Principal Component Analysis (PCA) on their spectra and observed that they closely overlapped in the first two principal components, making their separation challenging (Fig. 6(b)). Expanding the number of components did not significantly alter the results. Subse-

quently, we explored an alternative approach by clustering the pixels based on the reflectance code. The 2-D linear subspace of the reflectance code is depicted in Fig. 6(c). To quantitatively assess this improvement, we applied the K-means clustering algorithm to both the raw spectra space and the reflectance code latent space. We repeated this process 100 times with randomly sampled pixels from the classes. The results indicated that, on average, K-means clustering in the raw spectra space achieved an accuracy of 75.5%, while in the latent reflectance code space, it achieved 95.9%. This represents a substantial improvement of 20.4% in percentage accuracy. Even more challenging were the classes CP Hammock and CP/Oak Hammock (Fig. 6(d), 6(e)), which exhibited even closer proximity. In raw spectra space, the average clustering accuracy was 53.3%. In contrast, when we performed clustering in the REnc space, we obtained an accuracy of 89.9%, reflecting a notable improvement of 36.6%. In our comprehensive pairwise clustering experiment encompassing all ground truth classes within the scene, we observed an average improvement of 12.0% in classification accuracy across all class pairs. Notably, the most substantial improvements were evident among classes characterized by subtle differences. These pairwise enhancements are graphically illustrated in Fig. 7. These findings underscore the substantial effectiveness of REnc in capturing class-specific features essential for distinguishing between closely related classes.

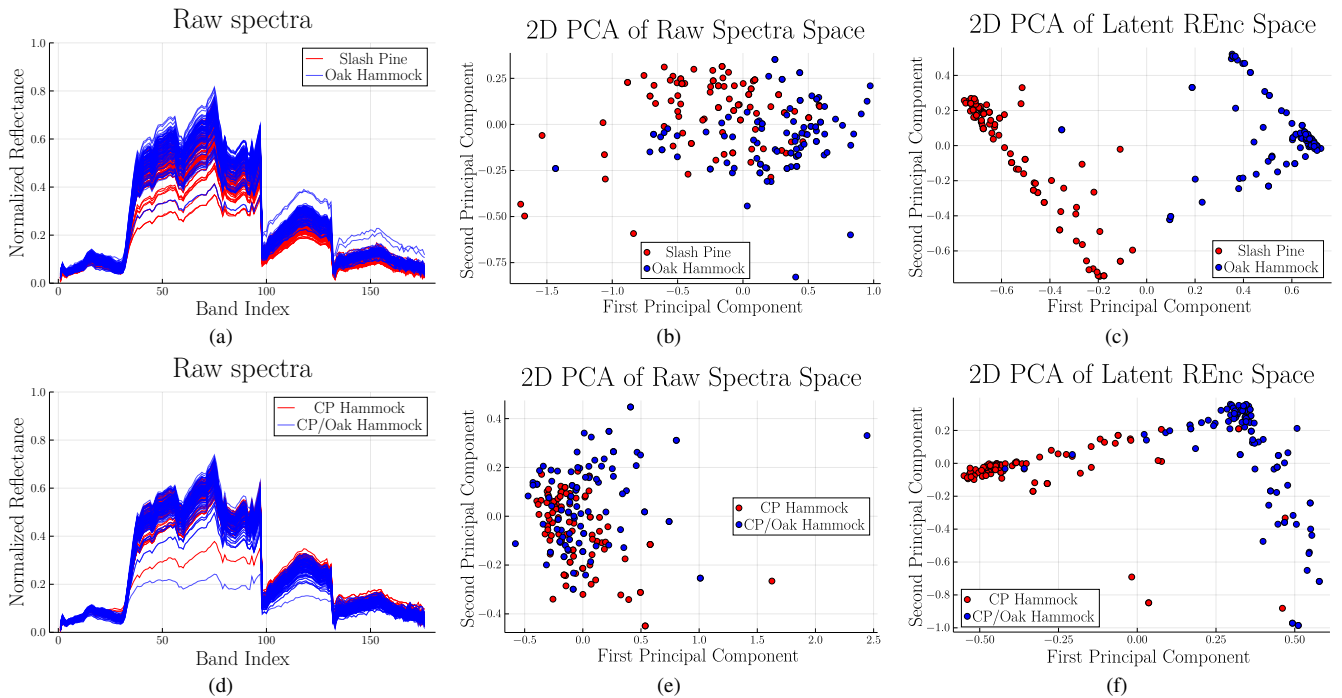


Fig. 6. SymAE allows for clustering pixels based on reflectance code, i.e.,  $\text{REnc}_1(D[\cdot])$  that is not affected by the atmospheric variations and other nuisance effects. (a,d) Raw spectra of spectrally close-by classes. (b,e) These classes are hard to separate in 2D raw spectra space. (c,f) Notice that the classes that otherwise have subtle differences in raw spectra are much easier to discriminate in latent coherent code space. Most significant improvement in the K-means clustering experiment we described is observed in classes with subtle differences like CP Hammock and CP/Oak Hammock depicted in (d), (e) and (f).

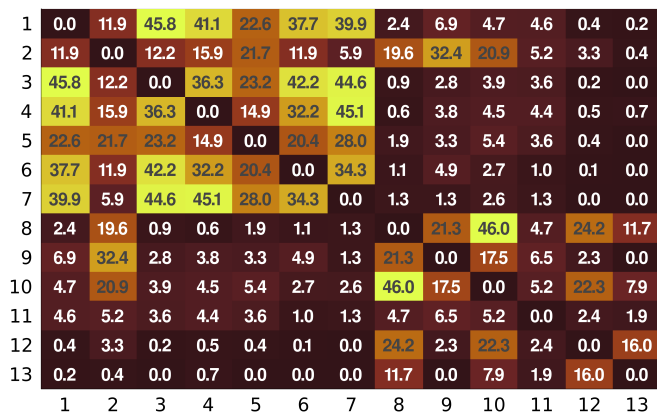


Fig. 7. Heatmap illustrating improvement in clustering in KSC dataset. The matrix elements indicate the percentage accuracy difference between K-means clustering in the latent reflectance code,  $\text{REnc}_1(D[.])$ , and clustering in the raw spectral data while doing pairwise unsupervised clustering between land-cover classes. The numbers on axes indicate the class indices, following same ordering as in Table I. This heatmap pertains to the ground truth-based training scenario and the clustering was done on test set. Pairs that show minimal improvement are those that already exhibit significant separation in raw spectra.

#### D. Using Surface-Reflectance Code: Classification

Building on the insights from the previous section, we focus on applying SymAE for HSI classification, utilizing the reflectance encoder  $\text{REnc}$  to extract class-specific information. We trained a feed-forward dense layer neural network with dropout regularization for ground truth class label prediction based on pixel reflectance codes. This pixel-by-pixel classification approach yielded an overall test accuracy of 94.65% in KSC scene. Our performance was compared with SpectralFormer, a state-of-the-art spectral classification architecture introduced by Hong *et al.* [17]. SpectralFormer, which leverages a modified Vision Transformer (ViT) [19] to utilize the sequential dependency of spectra, has demonstrated superiority over various models including KNN, Random

Forest, SVMs, 1D-CNN [33], RNN [34], MiniGCN [35], and ViT. Our experiments reveal that SymAE surpasses the pixel-based classification accuracy of SpectralFormer. The detailed results are presented in Table II. Additionally, we extended our evaluation to three widely recognized HSI benchmark datasets: Pavia University, Indian Pines, and Houston2013, with the results shown in Tables III, IV, and V respectively. The results indicate notable improvement in performance emphasizes SymAE’s strong proficiency in spectral feature extraction. As Sun *et al.* pointed out in their study [16], spectral features play a fundamental role in accurately characterizing the distribution of ground objects, serving as crucial discriminative factors in HSIs. The improved classification accuracy achieved by SymAE highlights its efficacy in HSI analysis, suggesting its utility for more precise and efficient mapping and monitoring tasks.

*Experiment Parameters:* For the Kennedy Space Center scene, we continued using the same network introduced in Section IV. The results of this network are presented in Table II. In this setup, both  $R_i$  and  $N_i$  were set to 64. We trained for 3000 epochs, dividing the data into 2048 mini-batches in each epoch, with a mini-batch size of 256. Additionally, SpectralFormer was trained for 1000 epochs using 3-band patches, with a learning rate and weight decay both set to 0.0005. For ViT, we trained for 3000 epochs with the same learning rate and no weight decay.

When training SymAE on the Pavia University, Indian Pines, and Houston2013 datasets, we set the dimensions of the latent codes,  $R_i$  and  $N_i$ , to 128 each, and trained for 4000 epochs. In each epoch, we divided the data into 2048 mini-batches, with each mini-batch containing 256 data points. For SpectralFormer and ViT on these datasets, we adhered to the configurations described by Hong *et al.* in their seminal work [17].

For additional details and code accessibility, including the architecture’s implementation and the data used, please refer to our GitHub repository at [https://github.com/archieb1999/SymAE\\_KSC](https://github.com/archieb1999/SymAE_KSC).

TABLE II  
Classification Results from Kennedy Space Center Dataset.

No.	Class	Training Samples	Test Samples	ViT	SpectralFormer (pixel based)	SymAE
1	Scrub	77	684	92.69 %	93.86 %	<b>95.61 %</b>
2	Willow Swamp	25	218	86.70 %	88.99 %	<b>96.79 %</b>
3	CP Hammock	26	230	<b>96.09 %</b>	94.35 %	85.22 %
4	CP/Oak Hammock	26	226	49.56 %	57.96 %	<b>80.53 %</b>
5	Slash Pine	17	144	61.81 %	56.94 %	<b>77.08 %</b>
6	Oak Hammock	23	206	42.23 %	42.23 %	<b>77.67 %</b>
7	Hardwood Swamp	11	94	76.60 %	59.57 %	<b>88.23 %</b>
8	Graminoid Marsh	44	387	85.27 %	90.18 %	<b>96.90 %</b>
9	Spartina Marsh	52	468	<b>97.44 %</b>	95.94 %	<b>97.44 %</b>
10	Typha Marsh	38	366	95.63 %	94.53 %	<b>97.27 %</b>
11	Salt Marsh	42	377	97.88 %	97.88 %	<b>98.14 %</b>
12	Mud Flats	47	456	87.06 %	94.52 %	<b>98.90 %</b>
13	Water Body	91	836	100.0 %	100.0 %	100.0 %
	Overall Accuracy			88.28 %	89.28 %	<b>94.65 %</b>
	Average Accuracy			82.23 %	82.07 %	<b>91.53 %</b>
	Kappa $\times 100$			86.95	88.06	<b>94.04</b>

TABLE III  
Classification Results from Pavia University Dataset.

No.	Class	Training Samples	Test Samples	ViT	SpectralFormer (pixel based)	SymAE
1	Asphalt	548	6304	77.19 %	87.34 %	<b>88.06 %</b>
2	Meadows	540	18146	67.32 %	77.12 %	<b>79.61 %</b>
3	Gravel	392	1815	67.77 %	54.93 %	<b>71.96 %</b>
4	Trees	524	2912	95.95 %	<b>97.73 %</b>	94.78 %
5	Painted metal sheets	265	1113	99.37 %	99.37 %	<b>99.64 %</b>
6	Bare soil	532	4572	89.85 %	92.67 %	<b>96.5 %</b>
7	Bitumen	375	981	87.46 %	86.14 %	<b>91.03 %</b>
8	Self blocking bricks	514	3364	85.17 %	<b>93.73 %</b>	90.49 %
9	Shadows	231	795	97.36 %	67.55 %	<b>98.74 %</b>
	Overall Accuracy			77.04 %	83.05 %	<b>85.76 %</b>
	Average Accuracy			85.37 %	84.06 %	<b>90.09 %</b>
	Kappa $\times 100$			70.99 %	78.11	<b>81.53</b>

TABLE IV  
Classification Results from Indian Pines Dataset.

No.	Class	Training Samples	Test Samples	ViT	SpectralFormer (pixel based)	SymAE
1	Alfalfa	15	31	77.42 %	<b>93.55 %</b>	87.10 %
2	Corn-notill	50	1378	60.89 %	57.76 %	<b>70.03 %</b>
3	Corn-mintill	50	780	60.51 %	<b>70.77 %</b>	69.10 %
4	Corn	50	187	78.61 %	<b>82.35 %</b>	<b>82.35 %</b>
5	Grass-pasture	50	433	90.99 %	91.69 %	<b>92.38 %</b>
6	Grass-trees	50	680	87.79 %	94.12 %	<b>95.0 %</b>
7	Grass-pasture-mowed	15	13	84.62 %	84.62 %	84.62 %
8	Hay-windrowed	50	428	96.73 %	96.73 %	<b>99.53 %</b>
9	Oats	15	5	80.00 %	60.00 %	<b>100.0 %</b>
10	Soybean-no-till	50	922	80.80 %	<b>82.00 %</b>	76.57 %
11	Soybean-min-till	50	2405	63.58 %	65.03 %	<b>67.98 %</b>
12	Soybean-clean	50	543	63.72 %	73.30 %	<b>77.90 %</b>
13	Wheat	50	155	<b>99.35 %</b>	98.71 %	<b>99.35 %</b>
14	Woods	50	1215	85.02 %	88.07 %	<b>89.30 %</b>
15	Buildings-Grass-Trees-Drives	50	336	50.00 %	53.57 %	<b>65.77 %</b>
16	Stone-Steel-Towers	50	43	100.0 %	100.0 %	100.0 %
	Overall Accuracy			72.43 %	74.94 %	<b>77.87 %</b>
	Average Accuracy			78.75 %	80.77 %	<b>84.81 %</b>
	Kappa $\times 100$			68.78	71.62	<b>74.84</b>

TABLE V  
Classification Results from Houston2013 Dataset.

No.	Class	Training Samples	Test Samples	ViT	SpectralFormer (pixel based)	SymAE
1	Healthy Grass	198	1053	83.76 %	<b>86.13 %</b>	84.05 %
2	Stressed Grass	190	1064	97.18 %	96.52 %	<b>98.68 %</b>
3	Synthetic Grass	192	505	99.80 %	99.80 %	<b>100.0 %</b>
4	Tree	188	1056	<b>98.77 %</b>	97.63 %	96.88 %
5	Soil	186	1056	98.01 %	<b>98.86 %</b>	<b>98.86 %</b>
6	Water	182	143	<b>98.60 %</b>	96.50 %	<b>98.60 %</b>
7	Residential	196	1072	77.52 %	86.01 %	85.35 %
8	Commercial	191	1053	56.98 %	52.90 %	<b>60.78 %</b>
9	Road	193	1059	67.52 %	64.59 %	<b>82.63 %</b>
10	Highway	191	1036	66.70 %	<b>93.34 %</b>	86.20 %
11	Railway	181	1054	68.41 %	73.15 %	<b>87.86 %</b>
12	Parking Lot1	192	1041	50.82 %	58.50 %	<b>83.38 %</b>
13	Parking Lot2	184	285	63.16 %	72.98 %	<b>78.25 %</b>
14	Tennis Court	181	247	<b>99.19 %</b>	98.79 %	98.79 %
15	Running Track	187	473	98.52 %	<b>98.73 %</b>	97.67 %
	Overall Accuracy			78.85 %	82.64 %	<b>87.68 %</b>
	Average Accuracy			81.66 %	84.96 %	<b>89.20 %</b>
	Kappa $\times 100$			77.10	81.20	<b>86.62</b>

*Ablation Analysis:* We conducted an ablation study by focusing on classes 3-6 from Table II of the KSC scene, identified as the most challenging to discriminate. For this analysis, all networks underwent training for 4000 epochs, each containing 64 mini-batches and a mini-batch size of 256, with data points being randomly reshuffled after each epoch. Post-training, classification was conducted using latent codes in a similar dense feed-forward network with dropout regularization as previously used. In configurations where both REnc and NEnc were employed, the latent code size was equally divided between them. The results, depicted in Fig. 8, indicate that utilizing both encoders concurrently results in reduced sensitivity to variations in latent code size and consistently yields higher accuracy.

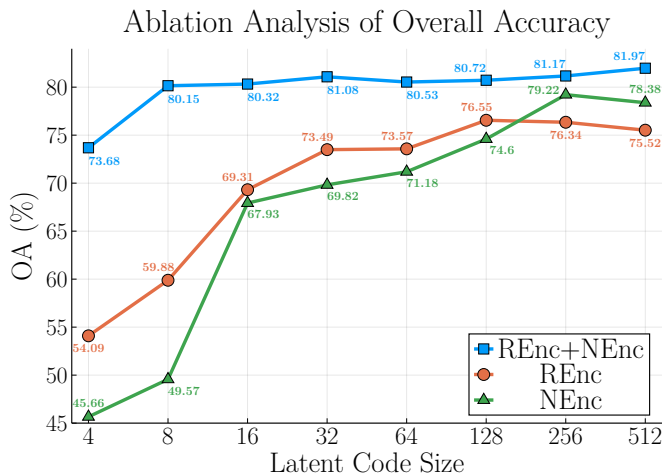


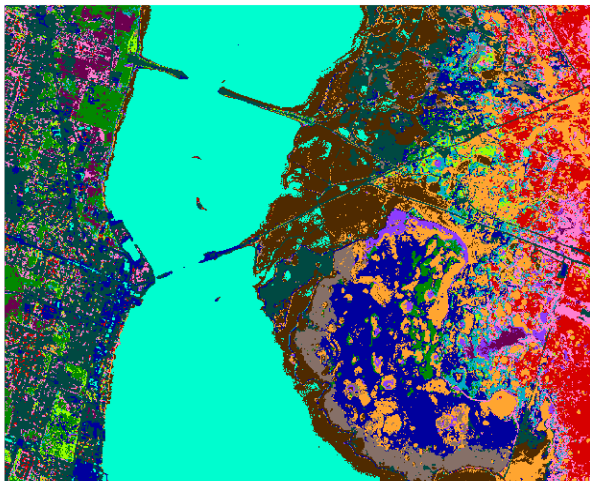
Fig. 8. Ablation study results for classes 3-6 in the KSC scene, highlighting the performance impact of employing both REnc and NEnc encoders. The graph demonstrates the reduced sensitivity to latent code size variations and the overall enhancement in classification accuracy when both encoders are used concurrently.

*Incorporating Spatial Information for Classification:* Our focus, so far, has predominantly been on spectral features. It is important to note, however, that purely spectral methods are susceptible to scattered noise, often leading to reduced accuracy levels. Spatial features, on the other hand, significantly contribute to HSI classification tasks by providing valuable local contextual information. Not surprisingly, recent leading HSI classification methods, such as SSRPnet [36] and CVSSN [37], adopt a spectral-spatial approach. While our purely spectral method achieved significant classification metrics, these results are still not on par with those of leading spectral-spatial methods, which currently set the best benchmarks. To compare SymAE with prominent HSI classification methods utilizing both spatial and spectral features, we integrated spatial information into our experiments. Our approach involved assigning labels to each pixel based on the mode of labels from its spectral feed-forward network and the labels of its eight adjacent neighbors, iterated three times for spatial smoothing. The results, presented in Table VI, show a marked improvement in accuracy. However, this naive

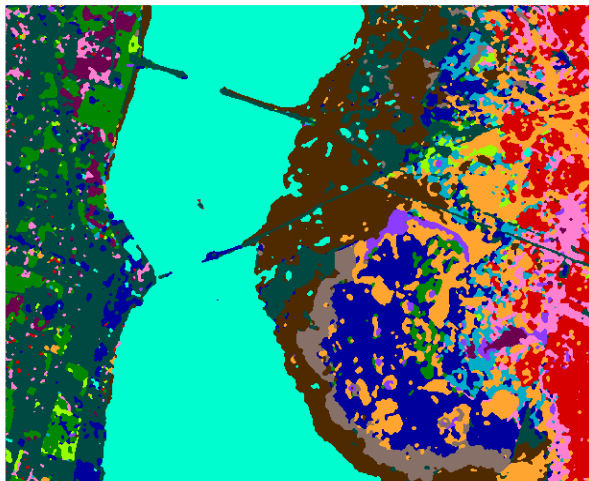
TABLE VI  
Classification Results Using SymAE Before and After Spatial Smoothing

HSI Scene	Metric	Pixel Based	Spatial Smoothing
Kennedy Space Center	OA	94.65 %	<b>99.48 %</b>
	AA	91.53 %	<b>99.09 %</b>
	$\kappa \times 100$	94.04	<b>91.43</b>
Pavia University	OA	85.76 %	<b>91.01 %</b>
	AA	90.09 %	<b>94.26 %</b>
	$\kappa \times 100$	81.53	<b>88.21</b>
Indian Pines	OA	77.87 %	<b>89.32 %</b>
	AA	84.81 %	<b>92.67 %</b>
	$\kappa \times 100$	74.84	<b>87.80</b>
Houston2013	OA	87.68 %	<b>89.89 %</b>
	AA	89.20 %	<b>91.05 %</b>
	$\kappa \times 100$	86.62	<b>89.02</b>

— Scrub    — Willow Swamp    — CP Hammock    — CP/Oak Hammock    — Slash Pine  
— Oak Hammock    — Hardwood Swamp    — Graminoid Marsh    — Spartina Marsh  
— Typha Marsh    — Salt Marsh    — Mud Flats    — Water Body



(a)



(b)

Fig. 9. Classification of SymAE-generated reflectance code for the Kennedy Space Center scene. a) Pixels are labeled using purely spectral information. b) Spatial smoothing applied to (a) which improved the classification accuracy.



approach to spatial smoothing may lead to distortions in accurately inferring the shapes of ground targets. These findings underscore SymAE’s potential in HSI classification and motivate further exploration into more sophisticated techniques for incorporating spatial information, potentially achieving even higher classification performance.

## V. TRAINING SYMAE WITHOUT GROUND TRUTH

Many remote sensing datasets lack ground truth labels for different spectra, making it challenging to group spectra before SymAE training. In such scenarios, we rely on the assumption of spatial correlation in the reflectance information, enabling us to group pixels located nearby within the scene. This assumption implies that spatially neighboring pixels likely belong to the same class.

This approach, which assumes that spatial proximity implies class similarity, provides structural organization to the data even when explicit labels are absent, costly to obtain, or difficult to acquire. This conjecture is particularly valid when dealing with datasets characterized by significant spatial correlation, as seen in examples like the Indian Pines dataset, which contains nearly 10 classes (farmlands) with extensive spatial coverage. Guided by this premise, we partitioned the KSC scene into small  $3 \times 3$  pixel groups for SymAE training. Our experiments on the KSC dataset revealed an average enhancement of 8.7% in pairwise K-means clustering accuracy, akin to the results discussed in subsection IV-C, when utilizing the reflectance code instead of raw spectra. It is crucial to note that we did not observe this improvement when spectra were randomly grouped within the scene. As expected, random spectral grouping led to significantly poorer clustering performance.

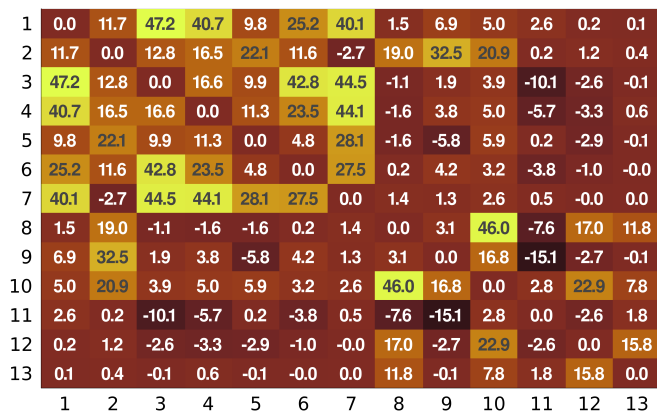


Fig. 10. Heatmap illustrating the improvement in K-means clustering achieved by utilizing the latent reflectance code in place of raw spectra, similar to Fig. 7, but without relying on ground truth labels. The heatmap highlights substantial performance enhancements across most classes, while also indicating instances of performance decline among specific class pairs.

The clustering analysis, as illustrated in Fig. 10, provides valuable insights into the performance of SymAE concerning pair-wise classes. We expect that the pixels situated close to class boundaries might not be well represented in SymAE’s latent space due to the simplicity of the grouping approach

employed. As evident, the performance of SymAE does exhibit variations across different classes. In fact, there is evidence of performance degradation for certain classes when compared to the use of raw spectra — most of these classes are not spatially contiguous or have a small extent.

This observation motivated us to verify this unsupervised approach further, in a more concentrated setting. We chose a small patch of land on the Indian Pines data set where our spatial-proximity assumption would seem to fit well. The patch primarily contains two close-by classes: Soybean-clean and Corn-min-till. The patch and the clustering analysis of the pixels are depicted in Fig. 11. In line with our prior observations from subsection IV-C, the initial representation of raw spectral data using the first two principal components does not reveal clear class separations. However, a substantial enhancement in structure becomes evident when examining the latent reflectance code space, where class distinctions become considerably more discernible. It is worth highlighting that pixels positioned near or along the class boundaries present a challenge in terms of differentiation. This observation aligns with our underlying assumption of spatial proximity, which groups border-adjacent pixels together prior to the SymAE training process, even if they genuinely belong to distinct classes. On a positive note, pixels situated at a greater distance from the class boundaries, or beyond their immediate vicinity, exhibit a distinct separation within the latent space. This facilitates their effective classification using a straightforward decision boundary. The results illustrate improved clustering within the latent space. This unsupervised grouping approach holds potential utility in settings where ground truth information is unavailable, such as remote or extraterrestrial environments. Future works directed towards developing more sophisticated and robust techniques for prior grouping in unsupervised contexts, offer a compelling ground for research.

## VI. DISCUSSION

In this section, we delve into the distinctive training phenomena observed during SymAE training, consider potential applications of this architecture, and outline areas with room for improvements.

### *Atypical Training Nature of SymAE*

We observed an intriguing phenomenon during the training process of SymAE. Initially, the training loss curve shows a decline, followed by an increase in loss. This is then followed by either a very gradual decrease or continued rise, ultimately reaching a state of saturation. Notably, this increase in loss corresponds with an improvement in K-means clustering performance within the latent space. We speculate that this phenomenon is attributable to the feature transfer dynamics between the encoding modules, specifically from NEnc to REnc, and the attention of decoder Fuse to them. In the early stages of SymAE training, NEnc inadvertently captures coherent reflectance features. As training progresses, dropout layers intermittently obfuscate these features. Consequently, Fuse works to extract information from REnc, which continually supplies data. Over time, Fuse adjusts to make



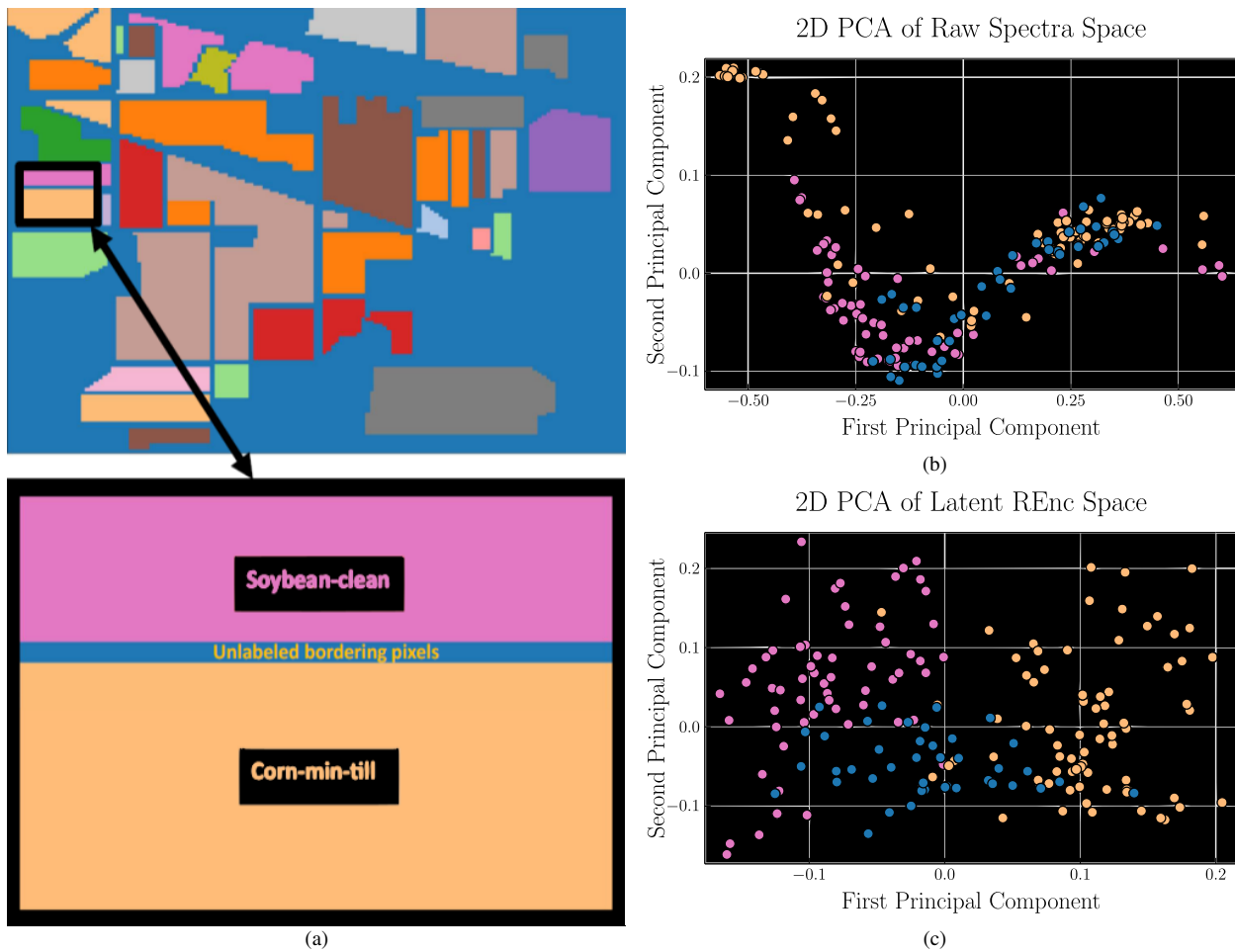


Fig. 11. A focused testing of SymAE without ground truth in Indian Pines scene. (a) A selected sub-region within the scene characterized by favorable spatial conditions to test SymAE without ground truth. (b) A 2D representation of the raw spectral space, utilizing the same color scheme as in (a) to visualize data points. (c) The 2D latent space of the reflectance code. Pixels near class boundaries pose challenges for differentiation, aligning with our spatial proximity assumption that groups border-adjacent pixels together. However, pixels farther from class boundaries exhibit clear separation within this space, aiding straightforward discrimination.

the most of REnc-sourced data. However, it is important to note that due to REnc’s inherent constraints, the quality of reconstruction falls short of what an unconstrained dense layer network can achieve. This discrepancy leads to the observed increase in loss during training. Having a sufficiently long nuisance code length can mitigate this atypical behavior, but that would significantly increase the number of training updates required to achieve effective disentanglement of nuisance and reflectance features in latent space. Empirically, we consistently achieved satisfactory performance of SymAE upon 3000 to 4000 training epochs with 2048 mini-batches, each mini-batch containing 256 datapoints in our experiments.

We would also like to highlight our selection of the Leaky ReLU with slope parameter 0.5 as activation function. Our decision in this regard was guided by empirical observations from our study. Throughout our investigations, we observed that traditional activation functions, including tanh and ReLU, exhibited susceptibility to vanishing gradient issues and the *dying ReLU* problem [38]. These challenges are particularly pronounced in SymAE, given its inherent stochastic nature. Our experimental results demonstrated that the Leaky ReLU,

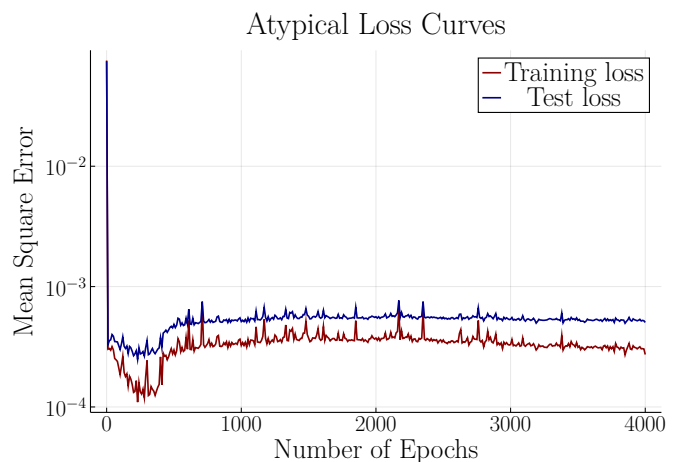


Fig. 12. Atypical training curves we encountered while training SymAE. At the outset, the training loss curve shows a descending trend, which is subsequently followed by a rise in loss, ultimately reaching a state of saturation.

characterized by its inherent flexibility, effectively mitigates these issues, thus establishing itself as the better choice for our network.

#### *Applications and Future Possibilities with SymAE*

SymAE presents a data-driven architecture with potential applications in challenging scenarios where physical modeling is impractical. For instance, we speculate, it can find utility in remote sensing tasks conducted in extraterrestrial environments or locations with limited information available about nuisance factors. SymAE offers an alternative approach that sidesteps the complexity associated with developing intricate physical models.

Some areas where SymAE could have implications and future applications include:

- **Atmospheric Correction Alternative and Data Quality Enhancement:** SymAE’s capacity to uniformize nuisance features like atmospheric interference through redatuming could make it work as a relative atmospheric correction method. This approach might enhance data quality in situations where physical modeling is not viable, although this potential needs further exploration.
- **Enhanced Hyperspectral Signature Analysis:** SymAE’s feature extraction and redatuming capabilities could enhance hyperspectral signature analysis, potentially aiding in finer material characterization and differentiation.
- **Scenario Exploration and Virtual Imaging:** The capability of SymAE to generate virtual images under varied conditions could be useful for scenario exploration and hypothesis testing, potentially aiding in more informed decision-making processes.
- **Data Augmentation and Model Training:** The generation of synthetic data by SymAE could be beneficial for machine learning model training, potentially enhancing model robustness, especially in situations with limited data.
- **Spatial-Spectral Fusion:** Future investigations can delve into effective integration of spatial information with spectral features, further extending SymAE’s utility in applications such classification and clustering.

#### *Scope for Improvement*

While SymAE has shown promising results, there are certain aspects that warrant further improvement:

- **Training Duration:** A significant consideration is the time required for effective disentanglement between reflectance and nuisance features. During our experiments, SymAE’s inherent stochastic nature usually necessitated around 6-8 million updates ( 9-12 hours on our devices) to satisfactorily disentangle these features, based on the configurations used for the datasets in this study. This extended training duration highlights the need for exploring more efficient training strategies and architectural refinements.
- **Initial Grouping Method in Unsupervised Scenarios:** The method employed for initial grouping in the fully unsupervised scenario of this study, while effective to a degree,

is relatively simplistic and prone to misclassifying pixels from different classes into a single group. Future work will focus on enhancing this grouping algorithm to reduce the likelihood of such misclassifications. Improving this aspect will bolster the overall robustness of the SymAE approach, especially in situations where ground truth labels are scarce or difficult to acquire.

## VII. CONCLUSION

This paper has introduced and detailed the Symmetric Autoencoder (SymAE), a novel approach for processing hyperspectral images. The primary objective of SymAE has been to effectively disentangle nuisance features from class-specific reflectance features within these images, utilizing a data-driven method leveraging symmetry under the reordering of pixels. Distinct from traditional denoising and atmospheric correction techniques, through the process of redatuming, SymAE has demonstrated capability in generating virtual hyperspectral images which can aid in analysis tasks. The results obtained from four benchmark HSI datasets have demonstrated the effectiveness of SymAE in enhancing clustering and classification tasks, emphasizing its spectral feature extraction capabilities. The methodology shows promise in addressing complexities within hyperspectral data by capturing pixel-level spectral characteristics. Furthermore, we propose an extension of SymAE to unsupervised scenarios. However, some areas require further investigation and refinement. Improving the a priori grouping algorithm’s robustness is essential for automation in unsupervised settings. We also acknowledge the time-intensive nature of achieving effective disentanglement, which warrants architectural refinements. Additionally, exploring the incorporation of spatial information into SymAE merits further research. In conclusion, the Symmetric Autoencoder architecture presents a tool with significant potential for hyperspectral image analysis, inviting deeper exploration and evaluation within the research community.

## VIII. ACKNOWLEDGEMENTS

All experimental procedures were conducted using the Julia programming language on a local computing system equipped with 128 GB RAM, an AMD Ryzen Threadripper 3960X 24-core processor, and a 24 GB NVIDIA GeForce RTX 3090 GPU. We would also like to acknowledge the use of ChatGPT, an AI language model developed by OpenAI, which played a significant role in refining portions of the text in this paper. The contributions of ChatGPT were valuable in enhancing the clarity and coherence of our writing. We would also like to thank the anonymous reviewers for providing valuable suggestions.

## REFERENCES

- [1] José M Bioucas-Dias, Antonio Plaza, Gustavo Camps-Valls, Paul Scheunders, Nasser Nasrabadi, and Jocelyn Chanussot, "Hyperspectral remote sensing data analysis and future challenges," *IEEE Geoscience and Remote Sensing Magazine*, vol. 1, no. 2, pp. 6–36, 2013.
- [2] Gary A Shaw and Hsiaohua K Burke, "Spectral imaging for remote sensing," *Lincoln laboratory journal*, vol. 14, no. 1, pp. 3–28, 2003.
- [3] Pedram Ghamisi, Naoto Yokoya, Jun Li, Wenzhi Liao, Sicong Liu, Javier Plaza, Behnood Rasti, and Antonio Plaza, "Advances in hyperspectral image and signal processing: A comprehensive overview of the state of the art," *IEEE Geoscience and Remote Sensing Magazine*, vol. 5, no. 4, pp. 37–78, 2017.
- [4] Behnood Rasti, Paul Scheunders, Pedram Ghamisi, Giorgio Licciardi, and Jocelyn Chanussot, "Noise reduction in hyperspectral imagery: Overview and application," *Remote Sensing*, vol. 10, no. 3, pp. 482, 2018.
- [5] Tian Han and David G Goodenough, "Investigation of nonlinearity in hyperspectral imagery using surrogate data methods," *IEEE Transactions on Geoscience and Remote Sensing*, vol. 46, no. 10, pp. 2840–2847, 2008.
- [6] Qiang Zhang, Yaming Zheng, Qiangqiang Yuan, Meiping Song, Haoyang Yu, and Yi Xiao, "Hyperspectral image denoising: From model-driven, data-driven, to model-data-driven," *IEEE Transactions on Neural Networks and Learning Systems*, 2023.
- [7] Qiang Zhang, Qiangqiang Yuan, Jie Li, Fujun Sun, and Liangpei Zhang, "Deep spatio-spectral bayesian posterior for hyperspectral image non-iid noise removal," *ISPRS Journal of Photogrammetry and Remote Sensing*, vol. 164, pp. 125–137, 2020.
- [8] Fengchao Xiong, Jun Zhou, Shuyin Tao, Jianfeng Lu, Jiantao Zhou, and Yuntao Qian, "Smds-net: Model guided spectral-spatial network for hyperspectral image denoising," *IEEE Transactions on Image Processing*, vol. 31, pp. 5469–5483, 2022.
- [9] Hongyan Zhang, Hongyu Chen, Guangyi Yang, and Liangpei Zhang, "Lr-net: Low-rank spatial-spectral network for hyperspectral image denoising," *IEEE Transactions on Image Processing*, vol. 30, pp. 8743–8758, 2021.
- [10] Bo-Cai Gao, Marcos J. Montes, Curtiss O. Davis, and Alexander F.H. Goetz, "Atmospheric correction algorithms for hyperspectral remote sensing data of land and ocean," *Remote Sensing of Environment*, vol. 113, pp. S17–S24, 2009, Imaging Spectroscopy Special Issue.
- [11] Jian Sun, Fangcao Xu, Guido Cervone, Melissa Gervais, Christelle Wauthier, and Mark Salvador, "Automatic atmospheric correction for shortwave hyperspectral remote sensing data using a time-dependent deep neural network," *ISPRS Journal of Photogrammetry and Remote Sensing*, vol. 174, pp. 117–131, Apr. 2021.
- [12] Mark A. Kramer, "Nonlinear principal component analysis using autoassociative neural networks," *AICHE Journal*, vol. 37, no. 2, pp. 233–243, 1991.
- [13] I Goodfellow, Y Bengio, and A Courville, *Deep learning*, MIT Press, 2016.
- [14] Pawan Bharadwaj, Matthew Li, and Laurent Demanet, "Redatuming physical systems using symmetric autoencoders," 2022.
- [15] Wim A Mulder, "Rigorous redatuming," *Geophysical Journal International*, vol. 161, no. 2, pp. 401–415, 2005.
- [16] Yifan Sun, Bing Liu, Xuchu Yu, Anzhu Yu, Pengqiang Zhang, and Zhixiang Xue, "Exploiting discriminative advantage of spectrum for hyperspectral image classification: Spectralformer enhanced by spectrum motion feature," *IEEE Geoscience and Remote Sensing Letters*, vol. 20, pp. 1–5, 2022.
- [17] Danfeng Hong, Zhu Han, Jing Yao, Lianru Gao, Bing Zhang, Antonio Plaza, and Jocelyn Chanussot, "Spectralformer: Rethinking hyperspectral image classification with transformers," *IEEE Transactions on Geoscience and Remote Sensing*, vol. 60, pp. 1–15, 2021.
- [18] Ashish Vaswani, Noam Shazeer, Niki Parmar, Jakob Uszkoreit, Llion Jones, Aidan N Gomez, Lukasz Kaiser, and Illia Polosukhin, "Attention is all you need," *Advances in neural information processing systems*, vol. 30, 2017.
- [19] Alexey Dosovitskiy, Lucas Beyer, Alexander Kolesnikov, Dirk Weissenborn, Xiaohua Zhai, Thomas Unterthiner, Mostafa Dehghani, Matthias Minderer, Georg Heigold, Sylvain Gelly, et al., "An image is worth 16x16 words: Transformers for image recognition at scale," *arXiv preprint arXiv:2010.11929*, 2020.
- [20] Xiaofei Yang, Weijia Cao, Yao Lu, and Yicong Zhou, "Hyperspectral image transformer classification networks," *IEEE Transactions on Geoscience and Remote Sensing*, vol. 60, pp. 1–15, 2022.
- [21] Wenxuan He, Weiliang Huang, Shuhong Liao, Zhen Xu, and Jingwen Yan, "Csit: A multiscale vision transformer for hyperspectral image classification," *IEEE Journal of Selected Topics in Applied Earth Observations and Remote Sensing*, vol. 15, pp. 9266–9277, 2022.
- [22] Weiliang Huang, Wenxuan He, Shuhong Liao, Zhen Xu, and Jingwen Yan, "Efficient spectralformer for hyperspectral image classification," *Digital Signal Processing*, vol. 143, pp. 104237, 2023.
- [23] George Papamakarios, Eric Nalisnick, Danilo Jimenez Rezende, Shakir Mohamed, and Balaji Lakshminarayanan, "Normalizing flows for probabilistic modeling and inference," *The Journal of Machine Learning Research*, vol. 22, no. 1, pp. 2617–2680, 2021.
- [24] Yang Liu, Saeed Anwar, Zhenyue Qin, Pan Ji, Sabrina Caldwell, and Tom Gedeon, "Disentangling noise from images: A flow-based image denoising neural network," *Sensors*, vol. 22, no. 24, pp. 9844, 2022.
- [25] Carl Doersch, "Tutorial on variational autoencoders," *arXiv preprint arXiv:1606.05908*, 2016.
- [26] Manzil Zaheer, Satwik Kottur, Siamak Ravanbakhsh, Barnabás Póczos, Ruslan Salakhutdinov, and Alexander J. Smola, "Deep sets," *Advances in Neural Information Processing Systems*, , no. ii, pp. 3392–3402, apr 2017.
- [27] Nitish Srivastava, Geoffrey Hinton, Alex Krizhevsky, Ilya Sutskever, and Ruslan Salakhutdinov, "Dropout: a simple way to prevent neural networks from overfitting," *The journal of machine learning research*, vol. 15, no. 1, pp. 1929–1958, 2014.
- [28] Steven M Adler-Golden, Michael W Matthew, Lawrence S Bernstein, Robert Y Levine, Alexander Berk, Steven C Richtsmeier, Prabhat K Acharya, Gail P Anderson, Jerry W Felde, JA Gardner, et al., "Atmospheric correction for shortwave spectral imagery based on modtran4," in *Imaging Spectrometry V*. International Society for Optics and Photonics, 1999, vol. 3753, pp. 61–69.
- [29] Joseph W Boardman, "Post-atrem polishing of aviris apparent reflectance data using effort: a lesson in accuracy versus precision," in *Summaries of the seventh JPL airborne earth science workshop*, 1998, vol. 1, p. 53.
- [30] Michael Innes, Elliot Saba, Keno Fischer, Dhairya Gandhi, Marco Concetto Rudilosso, Neethu Mariya Joy, Tejan Karmali, Avik Pal, and Viral Shah, "Fashionable modelling with flux," *CoRR*, vol. abs/1811.01457, 2018.
- [31] Pascal Vincent, Hugo Larochelle, Yoshua Bengio, and Pierre-Antoine Manzagol, "Extracting and composing robust features with denoising autoencoders," in *Proceedings of the 25th international conference on Machine learning*, 2008, pp. 1096–1103.
- [32] Chen Xing, Li Ma, Xiaoquan Yang, et al., "Stacked denoise autoencoder based feature extraction and classification for hyperspectral images," *Journal of Sensors*, vol. 2016, 2016.
- [33] Behnood Rasti, Danfeng Hong, Renlong Hang, Pedram Ghamisi, Xudong Kang, Jocelyn Chanussot, and Jon Atli Benediktsson, "Feature extraction for hyperspectral imagery: The evolution from shallow to deep: Overview and toolbox," *IEEE Geoscience and Remote Sensing Magazine*, vol. 8, no. 4, pp. 60–88, 2020.
- [34] Renlong Hang, Qingshan Liu, Danfeng Hong, and Pedram Ghamisi, "Cascaded recurrent neural networks for hyperspectral image classification," *IEEE Transactions on Geoscience and Remote Sensing*, vol. 57, no. 8, pp. 5384–5394, 2019.
- [35] Danfeng Hong, Lianru Gao, Jing Yao, Bing Zhang, Antonio Plaza, and Jocelyn Chanussot, "Graph convolutional networks for hyperspectral image classification," *IEEE Transactions on Geoscience and Remote Sensing*, vol. 59, no. 7, pp. 5966–5978, 2020.
- [36] Chunbo Cheng, Hong Li, Jiangtao Peng, Wenjing Cui, and Liming Zhang, "Hyperspectral image classification via spectral-spatial random patches network," *IEEE Journal of Selected Topics in Applied Earth Observations and Remote Sensing*, vol. 14, pp. 4753–4764, 2021.
- [37] Mingsong Li, Yikun Liu, Guangkuo Xue, Yuwen Huang, and Gongping Yang, "Exploring the relationship between center and neighborhoods: Central vector oriented self-similarity network for hyperspectral image classification," *IEEE Transactions on Circuits and Systems for Video Technology*, vol. 33, no. 4, pp. 1979–1993, 2022.
- [38] Lu Lu, Yeonjong Shin, Yanhui Su, and George Em Karniadakis, "Dying relu and initialization: Theory and numerical examples," *arXiv preprint arXiv:1903.06733*, 2019.